

RESEARCH ARTICLE

10.1002/2014JA020470

Key Points:

- Poynting Flux-conserving boundary conditions for global MHD models
- Consistency between magnetospheric Poynting flux and ionospheric Joule heating
- Hardwall boundary conditions introduce various artifacts to global MHD models

Supporting Information:

- Table S1 and Figures S1–S5

Correspondence to:

S. Xi,
sheng.xi.th@dartmouth.edu

Citation:

Xi, S., W. Lotko, B. Zhang, O. J. Brambles, J. G. Lyon, V. G. Merkin, and M. Wiltberger (2015), Poynting flux-conserving low-altitude boundary conditions for global magnetospheric models, *J. Geophys. Res. Space Physics*, 120, 384–400, doi:10.1002/2014JA020470.

Received 11 AUG 2014

Accepted 8 DEC 2014

Accepted article online 11 DEC 2014

Published online 27 JAN 2015

Poynting flux-conserving low-altitude boundary conditions for global magnetospheric models

S. Xi¹, W. Lotko¹, B. Zhang¹, O. J. Brambles¹, J. G. Lyon², V. G. Merkin³, and M. Wiltberger⁴

¹Thayer School of Engineering, Dartmouth College, Hanover, New Hampshire, USA, ²Department of Physics and Astronomy, Dartmouth College, Hanover, New Hampshire, USA, ³Johns Hopkins University Applied Physics Laboratory, Laurel, Maryland, USA, ⁴High Altitude Observatory, National Center for Atmospheric Research, Boulder, Colorado, USA

Abstract A method for specifying low-altitude or inner boundary conditions that conserve low-frequency, magnetic field-aligned, electromagnetic energy flux across the boundary in global magnetospheric magnetohydrodynamics (MHD) models is presented. The single-fluid Lyon-Fedder-Mobarry (LFM) model is used to verify this method, with comparisons between simulations using LFM's standard hardwall boundary conditions and the new flux-conserving boundary conditions. Identical idealized upstream solar wind and interplanetary magnetic field conditions and the same constant ionospheric conductance are used in both runs. The results show that, compared to LFM's standard hardwall boundary conditions, the flux-conserving method improves the transparency of the boundary for the flow of low-frequency (essentially DC) electromagnetic energy flux along field lines. As a consequence, the hemispheric integrated field-aligned DC Poynting flux just above the boundary is close to the hemispheric total Joule heating of the ionosphere, as it should be if electromagnetic energy is conserved. The MHD velocity and perpendicular currents are well-behaved near the inner boundary for the flux conserving boundary conditions.

1. Introduction

Global magnetohydrodynamic (MHD) modeling has become an important method for studying the near-Earth space environment. It provides a quantitative description of many important processes occurring in the magnetosphere, so it can facilitate both physical understanding and the possibility of numerical space weather prediction. Global MHD modeling of magnetospheres began about 35 years ago with the development of two-dimensional MHD models of the solar wind-magnetosphere interaction [Leboeuf *et al.*, 1978; Lyon *et al.*, 1980]. The first three-dimensional models were reported later by Brecht *et al.* [1982] and Ogino [1986]. A simple model for the conducting ionosphere was subsequently embedded as a low-altitude boundary condition on the 3-D model [Fedder and Lyon, 1987]. This model connects magnetosphere and ionosphere convection through the closure of field-aligned currents (FACs) in the ionosphere. The convection in the magnetosphere was shown to be controlled partly by the ionosphere in these simulations. Comparisons of direct measurements and model results were also carried out by Fedder and Lyon [1987] and Frank *et al.* [1995], validating the predictive ability of global models and confirming that they can provide a powerful and effective way to investigate the physics of the solar wind-magnetosphere-ionosphere system.

Continued development of global models has been steady. Global MHD models in common use today include the Lyon-Fedder-Mobarry (LFM) model [Lyon *et al.*, 2004], the Block-Adaptive-Tree Solar wind Roe-type Upwind Scheme (BATS-R-US) model [Powell *et al.*, 1999], the Open Geospace General Circulation (OpenGGCM) model [Raeder, 2003], the UCLA MHD code [Walker *et al.*, 2006], the Grand Unified Magnetosphere-Ionosphere Coupling Simulation (GUMICS) model [Janhunen *et al.*, 2012], the Japanese finite volume total variation diminishing (FV-TVD) MHD code [Tanaka, 1995], and the Chinese Lagrangian version of the piecewise parabolic method (PPMLR) MHD code [Hu *et al.*, 2007]. Some multifluid MHD models have also emerged: the Winglee MHD model [Winglee *et al.*, 2005], the multifluid Lyon-Fedder-Mobarry (MFLFM) model [Wiltberger *et al.*, 2010; Brambles *et al.*, 2010; Garcia *et al.*, 2010], and the multifluid BATS-R-US model [Glocer *et al.*, 2009]. Additional physics, such as Hall MHD and pressure anisotropy, can also be included in the global models [Tóth *et al.*, 2012].

Boundary conditions are a crucial part of any numerical model. For an n th order numerical scheme, conditions for $n/2$ (even n) or $(n + 1)/2$ (odd n) additional cells (ghost cells) on the boundary of the computational

domain are usually needed. Boundary conditions in a global MHD model include the conditions for scalar density and sound speed (or temperature or pressure), vector velocity (or momentum), and perturbation magnetic fields. Two different boundaries are present in global models: an outer boundary in the interplanetary medium and a low-altitude boundary surrounding the Earth.

The outer boundaries include an upstream boundary, a side boundary, and a downstream boundary. The upstream boundary is usually placed upstream from Earth about 30 Earth radii (R_E), where Dirichlet boundary conditions are specified on solar wind (SW) and interplanetary magnetic field (IMF) variables. The side and downstream boundaries are sufficiently far away that the solar wind velocity becomes super (MHD) fast after its interaction with the magnetosphere. Thus, the numerical artifacts they produce will minimally affect the solution in the region of interest. These conditions are usually in the form of Neumann boundary conditions, i.e., $\partial\xi/\partial n = 0$, where n is the coordinate normal to the boundary and ξ is any of the MHD variables.

The inner boundary in global MHD models in common use today is located at 2–4 R_E from the center of Earth. Thus, a gap exists between the ionosphere and the simulation boundary where the MHD equations are solved. The choice of location for this boundary is determined by numerical requirements and physical considerations. The numerical requirement arises from the fact that geomagnetic flux tubes converge very rapidly in the gap and even above it in the low-altitude magnetosphere. Resolution of convection electric fields and magnetically guided Alfvén waves in this region requires an increasingly fine-scale grid to avoid significant numerical diffusion. In addition as the grid gets finer, satisfying the Courant condition requires a very small time step. The requirements for a high-resolution grid in the gap and a short time step are numerically very demanding, so the physics in the gap region is treated differently than in the computational domain outside of it. The physical processes occurring in the gap region are actually highly non-MHD and include parallel electron acceleration and parallel and perpendicular ion acceleration, which lead to non-Maxwellian velocity distributions that strongly violate the MHD assumption.

The simplest treatment of the gap physics, on the spatial and temporal scales of interest in MHD, is to assume that field-aligned currents flow divergence free from the low-altitude simulation boundary to the ionosphere along dipole field lines where they close via collisional Pederson and Hall currents. The treatment of current closure in the ionosphere on MHD time scales of order 100 s or greater is described by Ohm's law, current continuity, and the electrostatic approximation [Lotko, 2004]. The resulting electric potential is derived from the well-known Poisson equation [Merkin and Lyon, 2010] and is typically mapped from the ionosphere along assumed equipotential dipole magnetic field lines to the low-altitude boundary. The perpendicular electric field and MHD velocity, $\mathbf{v}_\perp = \mathbf{v}_E = \mathbf{E}_\perp \times \mathbf{B}_d / B_d^2$, are calculated assuming a dipole magnetic field B_d in the gap. This velocity is imposed as a boundary condition on the MHD solver [Fedder and Lyon, 1987; Goodman, 1995].

In addition to the boundary condition on the perpendicular velocity, conditions on density (ρ), sound speed (c_s) (or pressure or temperature), perturbation magnetic field (\mathbf{B}_1), and parallel velocity (v_\parallel) must be specified. Less attention has been devoted to the physical specification of these boundary conditions, which are usually given as Dirichlet or Neumann boundary conditions.

Table 1 lists the low-altitude boundary conditions used in different global models as reported in the literature or communicated from the model users or architects. All include a model ionosphere that solves a Poisson equation for the ionospheric potential. Some of the models continue to be evolved with new physics, improved numerical techniques, and/or alternative boundary conditions, and readers are advised to contact the model developers for information on planned or future modifications.

The baseline BATS-R-US model assumes zero radial velocity in the ghost cells. The tangential velocity is obtained from the mapped $\mathbf{E} \times \mathbf{B}$ velocity derived from the ionospheric potential solution. A Neumann boundary condition is used for the perturbation magnetic field and the pressure. The density is set to a constant, typically 28 AMU/cm³. The field-aligned current (FAC) for use in deriving the ionospheric potential is calculated at 3 R_E . Tanaka [1995] places the inner boundary at 3 R_E . Parallel momentum $\mathbf{m}_\parallel = \rho \mathbf{v}_\parallel$ is assumed to be inversely proportional to r^2 as r varies, and the perpendicular momentum is set to $\rho \mathbf{v}_E$. The perturbation in the radial magnetic field $B_{1r} = 0$ and the tangential perturbation magnetic field B_{1t} are set by forcing the tangential boundary current to be zero. Density ρ and temperature T are set to constant values at the boundary when the momentum is upward, while Neumann boundary conditions for ρ and T are imposed

Table 1. Low-Altitude Boundary Conditions for Global Models That Solve a Poisson Equation for the Ionospheric Potential^a

MODEL	MHD Solver Order	r_b (R_E)	Number (n) or Mass (ρ) Density	Sound speed (c_s), Pressure (P) or Temperature (T)	Velocity (\mathbf{v}) Momentum (\mathbf{m})	Magnetic Field (\mathbf{B})
PPMLR-MHD <i>Hu et al.</i> [2007]	3	3	$n = n_b$	$P = P_b$	$\mathbf{v} = 0, r < r_b$ $\mathbf{v} = \mathbf{v}_E, r_b < r < r_{\text{FAC}}$	$\mathbf{B}_1 = 0$
GUMICS4 <i>Janhunen et al.</i> [2012]	1	3.7	$\rho(l(r)) = \rho(l(r_1))$	$P(l(r)) = P(l(r_1))$	$v_r = 0$ $\mathbf{v} = \mathbf{v}_E - \mathbf{v}_E \cdot \hat{\mathbf{r}}$	$\mathbf{B}_1(l(r)) = \mathbf{B}_1(l(r_1))$
LFM <i>Lyon et al.</i> [2004]	8	2	$\partial_r \rho = 0 \Rightarrow \rho(r_{1-n}) = \rho(r_n)$	$\partial_r c_s = 0 \Rightarrow c_s(r_{1-n}) = c_s(r_n)$	$\mathbf{v}_\perp(t = t_N) = \mathbf{v}_E$ at $r = r_1$, where $t_N = N t_{\text{MIX}}$ $v_r = 0 \Rightarrow v_r(r_{1-n}) = -v_r(r_n)$ $\partial_r v_t = 0 \Rightarrow \mathbf{v}_t(r_{1-n}) = \mathbf{v}_t(r_n)$	$\partial_r \mathbf{B}_1 = 0 \Rightarrow \mathbf{B}_1(r_{1-n}) = \mathbf{B}_1(r_n)$
BATS-R-US <i>Powell et al.</i> [1999]	2	2.5 typical	$n = n_b$	$\partial_r P = 0$	$v_r = 0$ $\mathbf{v} = \mathbf{v}_E - \mathbf{v}_E \cdot \hat{\mathbf{r}}$	$\partial_r \mathbf{B}_1 = 0$
OpenGGCM <i>Raeder</i> [2003]	4	3 typical	$n = n_b$	$T = T_b$	$\mathbf{v} = \mathbf{v}_E$	\mathbf{B} from Faraday using \mathbf{E} across boundary
FV-TVD <i>Tanaka</i> [1995]	2	3	$\rho = \rho_b, m_r > 0$ $\partial_r \rho = 0, m_r < 0$	$T = T_b, m_r > 0$ $\partial_r T = 0, m_r < 0$	$\partial_r(r^2 m_\parallel) = 0$ $\mathbf{m}_\perp = \rho \mathbf{v}_E$	$B_{1r} = 0$ $\partial_r(r \mathbf{B}_{1t}) = 0$

^aDefinitions and notes:

r = radius from the center of Earth in spherical coordinates. $\hat{\mathbf{r}}$ = radial unit vector. r_b = radius of low-altitude boundary. r_1 = radius of first active cell center.

r_n = radius of n th cell center. In LFM, $n = 1, 2, 3, 4$. $r_{1,2,3,4}$ = first four active cell centers; $r_{0,-1,-2,-3}$ = ghost cell centers.

r_{FAC} = radial location where FACs are calculated.

∂_r = derivative normal to the spherical low-altitude boundary.

l = coordinate along the magnetic field line. $l(r)$ = point on the field line at radius r .

n_b, ρ_b, T_b, P_b are constant values of the number density, mass density, temperature, and pressure specified in the ghost cells. Typical reported values are as follows:

$n_b = 370$ (PPMLR), 28 (BATS-R-US), 2 (OpenGGCM) all in AMU/cm^3 . $P_b = 0.0465$ nPa (PPMLR); $T_b = 200$ eV (OpenGGCM);

ρ_b, T_b not reported for FV-TVD.

$v_{t,r}$ = tangential, radial component of velocity. $v_{\parallel,\perp}$ = parallel, perpendicular component of velocity.

\mathbf{m} = momentum. $m_{\parallel,\perp}$ = parallel, perpendicular component of momentum. m_r = radial component of momentum.

$\mathbf{v}_E = \mathbf{E}_{\text{map}} \times \mathbf{B}_d / B_d^2$ = drift velocity derived from the ionospheric electric field mapped to the location where the condition is imposed.

\mathbf{B}_1 = perturbation magnetic field. $\mathbf{B}_{1t,r}$ = tangential, radial component of the perturbations magnetic field.

t_{MIX} = time interval (10 s typical) at which the solution from the LFM ionospheric solver is updated; $N = 0, 1, 2, \dots$

for inward momentum. The GUMICS-4 model copies ρ, P , and \mathbf{B}_1 along dipole magnetic field lines from the inner boundary cells at $r_b = 3.7 R_E$ to set values in the ghost cells, i.e., these quantities are constant along field lines [*Janhunen et al.*, 2012]. The velocity boundary condition for GUMICS-4 is the same as described in BATS-R-US. A simple hardwall boundary is used in the standard LFM model, where the normal velocity component (v_r) is reflecting (antisymmetric) across the spherical inner boundary located at $r_b = 2 R_E$, with all other variables except \mathbf{v}_\perp satisfying a Neumann boundary condition (symmetric) [*Lyon et al.*, 2004]. The perpendicular velocity is set to the electric drift velocity at the cell center of the first active cell above r_b each time the ionosphere solver MIX is called (exchange time); however, \mathbf{v}_\perp is allowed to float between MIX exchange times. OpenGGCM sets the density and temperature to constant values in the ghost cells below r_b where the velocity is set to the mapped $\mathbf{E} \times \mathbf{B}$ velocity derived from ionospheric potential. The magnetic field in the ghosts cells is derived from Faraday's law using the MHD electric field in the active region and the mapped ionospheric electric field in both the ghost cell region and the region below the nominal ghost cells for this calculation. *Hu et al.* [2007] place the inner boundary at $r_b = 3 R_E$. The FAC for use in deriving the ionospheric potential is taken from $r_{\text{FAC}} = 4.39 R_E$. At $r < r_b$ the velocity and perturbation magnetic field are set to zero, while the density and pressure are set to 370 cm^{-3} and 0.0465 nPa, respectively. In the region between r_b and R_{FAC} , the velocity is set to \mathbf{v}_E and the perturbation magnetic field \mathbf{B}_1 is determined by the MHD solver.

These various boundary conditions provide stable solutions to the MHD equations, but the solutions may exhibit nonphysical behavior near the artificial boundary. Thus, improvements in the specification of low-altitude boundary conditions are needed. In this paper, flux-conserving boundary conditions that conserve electromagnetic energy flux along geomagnetic field lines are developed and verified. Metrics for evaluating the improvements in the solution for velocities and the perturbation magnetic fields are

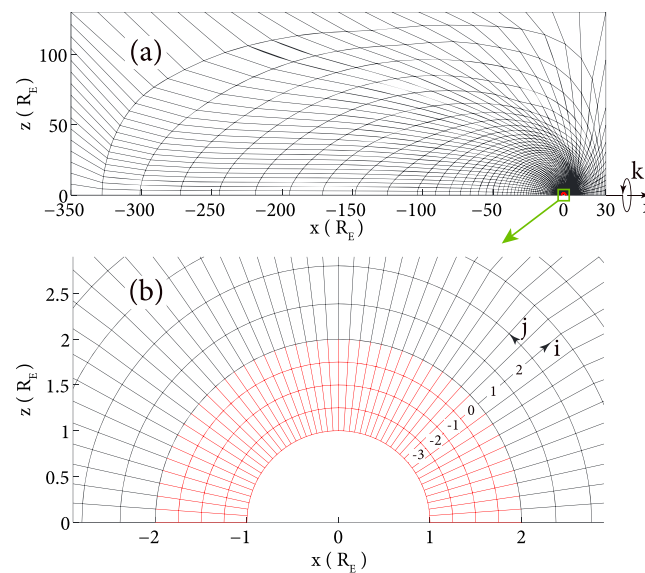


Figure 1. A constant k plane of the LFM grid. (a) A full k plane grid. (b) Zoomed-in grid near the low-altitude boundary is at $2 R_E$. Additional ghost cells (red) are required below the active cells (black). The radial distances for the $i = 2, 3, 4$ shells are $2.38 R_E$, $2.77 R_E$, and $3.17 R_E$, respectively.

presented. The approach involves setting the velocity to the $\mathbf{E} \times \mathbf{B}$ drift velocity in the ghost cells. The boundary condition on the perturbation magnetic field in the ghost cells assumes that $\mathbf{B}_\perp/B_d = \text{const}$ (B_d is the dipole magnetic field), which is valid on MHD time scales when $\mu_0 \Sigma_p v_A \gg 1$, where Σ_p is the Pederson conductance in the ionosphere, v_A is the smallest value of the Alfvén speed in the ghost cells, and μ_0 is the permeability of free space [Lotko, 2004]. In this limit, $\mathbf{B}_\perp/B_d = \text{const}$ is equivalent to assuming $j_\parallel/B_d = \text{const}$ [Lotko, 2004]. The electrodynamic part of the MHD solution near the inner boundary is significantly improved by this boundary condition. Electromagnetic energy flux flowing along field lines through the inner boundary is nearly conserved and is consistent with the distribution and intensity of Joule dissipation in the ionosphere. This method provides an

improvement in the treatment of inner boundary conditions in single-fluid global MHD models, and it may also be applicable to multifluid models. The LFM model is used to demonstrate the implementation and verification. However, this method should also be useful for the other models.

2. Model Descriptions

2.1. The LFM Global Model

The LFM model [Lyon *et al.*, 2004] is used to investigate the effects of different boundary conditions on the coupled, global magnetosphere-ionosphere system. It solves the time-dependent, ideal MHD equations numerically in semiconservative form (conservation of density, momentum, plasma energy, and magnetic flux) to obtain the state of the magnetosphere. This magnetosphere model is driven by SW and IMF data specified at the upstream boundary. A point dipole is placed at the center of the Earth to approximate the geomagnetic field. The LFM magnetosphere is coupled to a height-integrated 2-D polar ionosphere model. The FACs in the $i = 2$ shell (see Figure 1b) deduced from Ampere’s law are mapped along field lines to the ionosphere to serve as a source for the ionospheric potential equation [Merkin and Lyon, 2010]. The ionospheric potential is then solved and mapped to the LFM’s low-altitude boundary to obtain the electric field and from it the perpendicular velocity there.

The LFM grid is a distorted spherical grid azimuthally symmetric about the x axis (Sun-Earth line) of the solar magnetic coordinate system [Russell, 1971], in which i, j , and k represent the distorted radial, polar, and azimuthal direction, respectively. The grid with intermediate resolution ($i \times j \times k = 53 \times 48 \times 64$) on a constant k plane is shown in Figure 1a. Distortions in the grid, e.g., at lower altitude achieve higher resolution where the MHD solution requires it. The Sun is in the $+x$ direction. The 3-D grid structure can be constructed by rotating the constant k plane around the x axis in discrete azimuthal steps. The computational domain of the LFM model spans from $30 R_E$ sunward to $-350 R_E$ tailward and $130 R_E$ out to the side. A zoomed-in view of the k plane is shown in Figure 1b, where the distorted radial and polar directions are denoted by i and j . The first active cell just above the LFM low-altitude boundary is denoted by $i = 1$ and has its bottom surface located at a constant radius of $2 R_E$.

LFM uses eighth-order spatial differencing, which requires four ghost cells below the inner boundary, as shown by the red grid ($i = -3, -2, -1, 0$) in Figure 1b. The LFM active cells ($i = 1, 2, \dots$) are denoted by black grid in Figure 1b. For standard LFM boundary conditions, symmetric conditions with $\xi(i, j, k) = \xi(1 - i, j, k)$ are imposed, for density, sound speed, and perturbation magnetic fields. At exchange periods when the

ionosphere solver MIX is called, FACs are calculated at the $i = 2$ shell using Ampere's law. These currents are mapped to the ionospheric altitude at 120 km along dipole magnetic field lines using $j_{\parallel}/B_d = \text{const}$. The FAC is used in the 2-D potential equation described below to calculate the potential on the 2-D ionosphere [Merkin and Lyon, 2010]. By assuming zero parallel electric field in the gap region, the ionospheric potential is then mapped up to the cell vertices of the $i = 1$ shell. The electric drift velocity is then calculated from the mapped potential and imposed on the cell centers this shell. The drift velocity from the ionosphere potential is only imposed on the $i = 1$ shell at the exchange periods. At the times on and between the exchange periods, a symmetric condition is used for the tangential component of the velocity, while the antisymmetric condition is used for the boundary normal or radial component, i.e.,

$$v_r(i, j, k) = -v_r(1 - i, j, k) \quad (1)$$

and

$$v_t(i, j, k) = v_t(1 - i, j, k) \quad (2)$$

for $i = -3, -2, -1, 0$, where v_r is the velocity component in the radial direction (normal component) and v_t is the velocity component tangential to the low-altitude boundary. In addition, the ionospheric potential is mapped along field lines to the bottom of the $i = 1$ shell to determine the tangential electric field there for evolving Faraday's law on the active shells near the boundary. The tangential electric field from MIX is potential, which leads to $\partial B_r / \partial t = 0$ on $i = 1$. Also, this tangential electric field is kept constant between the MIX calls.

2.2. Flux-Conserving Boundary Conditions

Various artificial effects that corrupt the MHD solutions near the low-altitude boundary and introduce nonphysical effects in the MI coupling process result from the use of nonphysical low-altitude boundary conditions in global MHD models. Thus, improvements in the specification of the inner boundary conditions are needed.

As discussed in section 1, the perpendicular current in the gap region between the ionosphere and the low-altitude boundary of magnetosphere, where the ghost cells of the computational grid reside, may be neglected. In this case, we have [Lotko, 2004]

$$\nabla_{\parallel} \times \mathbf{B}_{\perp} = 0, \quad (3)$$

$$\nabla_{\perp} \times \mathbf{B}_{\perp} = \mu_0 \mathbf{j}_{\parallel}, \quad (4)$$

where \mathbf{B}_{\perp} is the perturbation magnetic field perpendicular to the dipole field lines and \mathbf{j}_{\parallel} is the FAC in the gap region. In dipole coordinates (ϕ, ν, μ) , where ϕ is the azimuthal direction, $\mu = \cos \theta / r^2$ is the parallel direction along a dipole magnetic field line, and $\nu = \sin^2 \theta / r$ fulfills the right-hand rule. In these coordinates (3) becomes $\frac{1}{h_{\phi} h_{\mu}} \partial_{\mu} (h_{\phi} B_{\phi}) = 0$ and $\frac{1}{h_{\nu} h_{\mu}} \partial_{\mu} (h_{\nu} B_{\nu}) = 0$. The metric scale factors $h_{\phi, \nu, \mu}$ for dipole geometry are defined as $h_{\phi} = r \sin \theta$, $h_{\nu} = r^2 / \sin \theta (1 + 3 \cos^2 \theta)^{1/2}$, and $h_{\mu} = h_{\phi} h_{\nu}$. These relations imply on a dipole field line [Lotko, 2004]

$$h_{\phi} B_{\phi} = \text{const}, \quad (5)$$

$$h_{\nu} B_{\nu} = \text{const}. \quad (6)$$

Hence, as long as the perpendicular magnetic field in the magnetosphere near the low-altitude boundary is known, the magnetic field in the gap region can also be calculated by mapping the perpendicular magnetic field down along field lines according to equations (5) and (6). The dipole mapping in the LFM model with intermediate resolution is shown in Figure 2. The blue and green lines are dipole magnetic field lines that connect to the grid centers of the $i = 1$ active shell, where the perpendicular components of the perturbation magnetic fields B_{ϕ} and B_{ν} are known from the MHD solver. These perturbation magnetic fields are then mapped from cell centers of the $i = 1$ shell along dipole field lines according to equations (5) and (6) to the center altitudes of the four ghost shells. The perturbation magnetic field on the ghost cell centers above the green field lines are set by the interpolation from the mapped values on the dipole field lines.

Note that in the region below the green field lines in Figure 2, indicated by the dark shadow, the ghost cells and active cells are not magnetically connected. The perturbation magnetic field in the dark region is expected to be small and is simply set to zero since the FACs flow mainly in the high-latitude polar region.

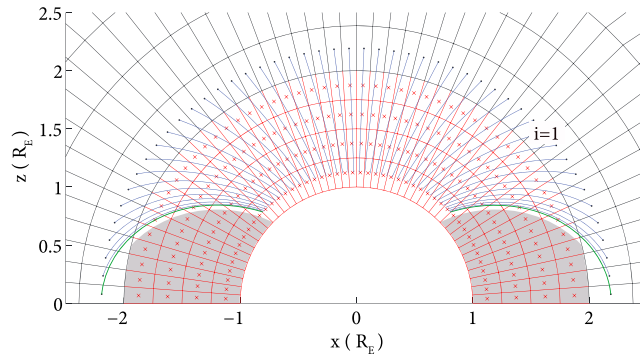


Figure 2. The mapping of perturbation magnetic fields. The blue and green lines are dipole field lines connecting the cell centers of the $i = 1$ shell. The perturbation magnetic fields are mapped along these field lines to the ghost cells and interpolated to the cell centers (red “x”) of the ghost cells above the green field lines. The perturbation magnetic fields in the region below the green field lines are set to zero.

The perpendicular current in the gap region can be neglected, with the curl of the perturbed parallel magnetic field being much smaller in magnitude than that of the perturbed perpendicular magnetic field [Lotko, 2004]. Then the parallel component of the perturbation magnetic field in the gap region can be set to zero for simplicity, with little effect on the flux-conserving property of the boundary. This zero-parallel magnetic field is consistent with the potential electric field from the ionospheric solver imposed in the gap region.

The ionosphere and MI gap region are treated in the electrostatic approximation in all global simulations. Let $\bar{\Sigma}$

represent the height-integrated ionospheric conductivity tensor [see Merkin and Lyon, 2010]; let Φ_i , $\mathbf{E}_{\perp i}$ and $\mathbf{J}_{\perp i}$ represent, respectively, the electrostatic potential, electric field, and height-integrated perpendicular current in the ionosphere; and let $j_{\parallel i}$ represent the field-aligned current mapped along dipole field lines to the top of the ionospheric conducting layer. When the height-integrated Ohm’s law, $\mathbf{J}_{\perp i} = \bar{\Sigma} \cdot \mathbf{E}_{\perp i}$, is combined with the height-integrated current continuity equation, $j_{\parallel i} = -\nabla \cdot \mathbf{J}_{\perp i}$, and the electrostatic approximation, $\mathbf{E}_i = -\nabla\Phi_i$, the ionospheric potential is determined by

$$\nabla \cdot \bar{\Sigma} \cdot \nabla\Phi_i = j_{\parallel i} \cos \delta. \tag{7}$$

Here δ is the magnetic field dip angle (local angle between the dipole magnetic field and the radial direction). Provided $\mu_0 \Sigma_p V_A \gg 1$, the current density \mathbf{j}_{\perp} perpendicular to the geomagnetic field is very small in the low-altitude magnetosphere and can be neglected [Lotko, 2004]. Thus, $\nabla \cdot \mathbf{j}_{\parallel} = 0$ in the gap region, and the rule for mapping the FAC from the magnetosphere model to the ionosphere is $j_{\parallel}/B_d = \text{const}$.

In the gap region, the field-aligned electric field is assumed to be zero in what follows, although this assumption can be relaxed. Thus, the potential distribution in the ghost cell grid can be determined by mapping the ionospheric potential upward along field lines connected to the ionosphere, and the electric field in the ghost cells can be easily calculated. Plasma motion perpendicular to the dipole magnetic field is set to the electric drift velocity, so the perpendicular velocity in the ghost cells can then be obtained

$$\mathbf{v}_E = \mathbf{E}_{\text{map}} \times \mathbf{B}_d / B_d^2, \tag{8}$$

where \mathbf{E}_{map} is the mapped electric field in the ghost cells and \mathbf{B}_d is the background dipole magnetic field. The parallel velocity in the ghost cells could be specified by an outflow model. It is set to zero in the results presented here. In the dark region in Figure 2, the ghost cells and the ionosphere are not magnetically connected to the active computational domain, and no ionospheric potential solution is available in this region. However, because FACs are weak in the low-latitude ionosphere, the potential in this region is set to zero, which results in zero velocity in this region. This feature agrees with the fact that the velocity in the low-latitude region is typically very small (neglecting corotation which is not included here).

The ϕ component of the electric field is determined from $h_{\phi} E_{\phi} = -\partial_{\phi}\Phi$. The potential in the gap region Φ is a constant on a single field line, so the integral between two fixed field lines separated in the azimuthal coordinate by $\Delta\phi$ will be

$$\begin{aligned} \int_{\phi_0}^{\phi_0+\Delta\phi} d\phi h_{\phi} E_{\phi} &= - \int_{\phi_0}^{\phi_0+\Delta\phi} d\Phi \\ &= -(\Phi(\phi_0 + \Delta\phi) - \Phi(\phi_0)), \end{aligned} \tag{9}$$

which is a constant for a fixed ϕ_0 . Thus, between the two field lines

$$h_\phi E_\phi = \text{const.} \quad (10)$$

Similarly,

$$h_\nu E_\nu = \text{const.} \quad (11)$$

The field-aligned Poynting flux flowing down to the ionosphere is

$$\begin{aligned} S_{\parallel} &= (E_\phi B_\nu - E_\nu B_\phi) / \mu_0 \\ &= (h_\phi E_\phi h_\nu B_\nu - h_\nu E_\nu h_\phi B_\phi) / (\mu_0 h_\phi h_\nu). \end{aligned} \quad (12)$$

The numerator is a constant as a consequence of equations (5) and (6) and equations (10) and (11). For a dipole field, $h_\phi h_\nu B_d = \text{constant}$ because $h_\phi h_\nu$ measures the area of a dipole flux tube. Thus, $S_{\parallel} / B_d = \text{const}$, which means that the field-aligned electromagnetic energy flux is conserved along dipole magnetic field lines when the boundary conditions proposed here are used to specify the velocity and perturbation magnetic field. We refer to this type of boundary condition as a flux-conserving boundary condition, and specifically here as a Poynting flux-conserving boundary condition.

Density and sound speed boundary conditions are needed to complete the boundary conditions at the low-altitude boundary. In the results shown in this paper, a simple condition to enforce pressure balance along magnetic field lines is used. Pressure along the field lines in the gap region shown in Figure 2 is set to the pressure determined from the MHD solution at $i = 1$ and then interpolated to the ghost cell centers. However, the pressure in the dark region cannot be obtained by a simple interpolation. The pressure in the dark region is set to the average of the values on the green field lines bordering the dark region, in the Northern and Southern Hemispheres. Density is also mapped as a constant along field lines, constrained by the MHD density in the $i = 1$ cell. These values are interpolated to the ghost cell centers using the same method as pressure. Then the sound speed in the ghost cells is calculated using the known pressure and density. Alternatively, one could also specify the density and sound speed conditions using other methods, such as the methods listed in Table 1, or using empirical models, e.g., using Global Core Plasma Model [Gallagher *et al.*, 2000] for the density conditions in the gap region. The effects of different methods to specify the density and sound speed conditions will not be discussed in this paper.

2.3. Simulation Setup

To evaluate the effects of flux-conserving boundary conditions and compare the differences in the MHD solution resulting from flux-conserving boundary conditions versus the standard LFM boundary conditions given in Table 2, two test simulations were run for identical SW/IMF conditions at the sunward boundary but with different low-altitude boundary conditions. The SW/IMF conditions are steady with $v_x = 400$ km/s, $v_y = v_z = 0$, plasma density, $n_{SW} = 5 \text{ cm}^{-3}$, sound speed, $c_s = 40$ km/s, and $B_z = -5$ nT, $B_x = B_y = 0$. Before the steady SW/IMF conditions are imposed on the sunward boundary, the magnetosphere is preconditioned for 4 h in both runs. During the preconditioning period, solar wind velocity, density, and sound speed are the same as the steady solar wind conditions, while IMF is set to southward with $B_z = -5$ nT in the first 2 h and switches to northward with $B_z = 5$ nT during the next 2 h. $B_x = B_y = 0$ for the entire runs. The initial sequence of south-to-north-to-south IMF B_z turnings reduces memory of initial conditions and populates the magnetosphere with solar wind plasma to produce a more realistic magnetospheric configuration. After the preconditioning period, each run is driven by the same steady SW/IMF conditions for 4 h with $B_z = -5$ nT. The simulation results shown in the following sections are derived from the simulation data within the last hour of each run, well after the recovery from the substorm initiated by the last southward turning. Only results from the Northern Hemisphere are shown because the geomagnetic field is represented in the simulation as an ideal dipole magnetic field without dipole tilt. Thus, the results for Northern and Southern Hemispheres are essentially symmetric. An intermediate grid resolution of $i \times j \times k = 53 \times 48 \times 64$ is used for these runs.

The 2-D ionospheric model in the simulations solves for the ionospheric potential from the mapped magnetospheric FACs using (7). The ionosphere spans the polar cap and extends to a lower magnetic latitude of 44° in both hemispheres. The ionosphere grid resolution is $2^\circ \times 2^\circ$ in the azimuthal and polar directions. The ionospheric conductances are set to constants, with Pedersen conductance $\Sigma_p = 5$ S and Hall conductance

Table 2. Boundary Conditions for the Test Runs^a

Runs	Mass Density (ρ)	Sound Speed (c_s)	Velocity (\mathbf{v})	Magnetic Field (\mathbf{B})
Run 1 Hardwall BCs	$\rho(r_{1-n}) = \rho(r_n)$	$c_s(r_{1-n}) = c_s(r_n)$	$v_r = 0 \Rightarrow v_r(r_{1-n}) = -v_r(r_n)$ $\partial_r \mathbf{v}_t = 0 \Rightarrow \mathbf{v}_t(r_{1-n}) = \mathbf{v}_t(r_n)$ $\mathbf{v}_\perp(t = t_N) = \mathbf{v}_E$ at $r = r_1$, where $t_N = Nt_{\text{MIX}}$	$\mathbf{B}_1(r_{1-n}) = \mathbf{B}_1(r_n)$
Run 2 Flux-conserving BCs	$\rho(l(r)) = \rho(l(r_1))$	$c_s(l(r)) = c_s(l(r_1))$	$\mathbf{v} = \mathbf{v}_E$, ($r < r_b$) $v_\parallel = 0$	$h_\phi B_\phi = \text{const}$ $h_\nu B_\nu = \text{const}$

^aDefinitions in this table are the same as for Table 1.

$\Sigma_H = 0$. The Hall conductance drops out of the solution for any constant value of Σ_H . The ionosphere evolves slowly compared to the MHD variability in the magnetosphere. The ionosphere solver is thus called only at 10 s intervals when the electric field is updated in the ghost region from which the boundary condition for the electric drift velocity is derived. This updating interval is called the “MIX exchange time.” Decreasing the MIX exchange time produces less mismatch between the state of ionosphere and magnetosphere between exchange times, so the simulation results will be more accurate. However, solving the ionosphere potential more frequently requires more computational time. The MIX exchange time is typically set to 10 s in LFM, which provides a good compromise between efficient run speed and accuracy of the solution.

3. Results and Discussion

A hardwall boundary condition introduces artificial effects in the MHD solution, especially in the region near the low-altitude boundary. These effects are also manifest in the coupling between the magnetosphere and ionosphere. They can be significantly reduced with flux-conserving boundary conditions.

3.1. Reduction of Artificial Effects Near the Low-Altitude Boundary

For the standard LFM boundary condition, at the MIX exchange time the MHD solver pauses, the ionosphere solver is called, and the value of \mathbf{v}_\perp is overwritten at cell centers in the $i = 1$ shell (first active cells) with the value derived from the ionosphere solver. The electric field \mathbf{E} derived from the ionosphere solver is also projected onto the bottom cell edges at the boundary (bottom of the $i = 1$ cells) at the exchange time, and this projected value replaces the electric field that was imposed there at the last MIX exchange time. The electric field imposed on $i = 1$ shell is electrostatic and is not updated on the bottom cell edges from Ohm’s law by the MHD solver. The MHD solver then continues with a hardwall condition on v_r and a free boundary condition on \mathbf{v}_t (Table 2) in the $i = 1$ cells to drift away from the constraint imposed by the ionosphere at the MIX exchange time. This boundary condition is referred to as “hardwall” in subsequent analysis.

For the Poynting flux-conserving boundary condition, the MHD solver also pauses at the MIX exchange time, but the values of \mathbf{v}_\perp derived from the ionosphere solver are imposed only in the four ghost cells ($i = 0, -1, -2, -3$) using the mapping and interpolation procedures described in section 2.2. These ghost-cell values of \mathbf{v}_\perp are held constant until the next MIX exchange time. No MHD variables are modified in the active region. In addition, the value of perturbation \mathbf{B}_\perp at the $i = 1$ cell centers is mapped downward along dipole field lines according to equations (5) and (6) and is then interpolated onto ghost cells at each MHD time step following the procedures described in section 2.2. The electric field on the bottom of $i = 1$ shell is calculated by the MHD solver using the velocity and magnetic field in the ghost cells and the first four active cells, which is different from the standard LFM boundary condition for electric field described previously. For this new boundary condition, the electric field on the $i = 1$ surface is inductive, in contrast with the standard LFM boundary condition, which imposes the electrostatic field from MIX on the $i = 1$ surface at MIX exchanges and maintains it at this value between MIX exchanges.

Figures 3a and 3b show the time variation of the three components of the velocity vector near the north magnetic pole and at the location $\phi = 17.9^\circ$, $\theta = 19.7^\circ$ (magnetic latitude (MLAT) = 70.3° , magnetic local time (MLT) = 13:12 h), respectively, on the $i = 1$ shell at a 1 s cadence. The red curves are for the standard LFM hardwall boundary condition. Blue curves are for the Poynting flux-conserving boundary condition. The results shown in Figure 3 are from 7:00 to 7:01 simulation time (ST), when the IMF has been -5 nT for 3 h. The

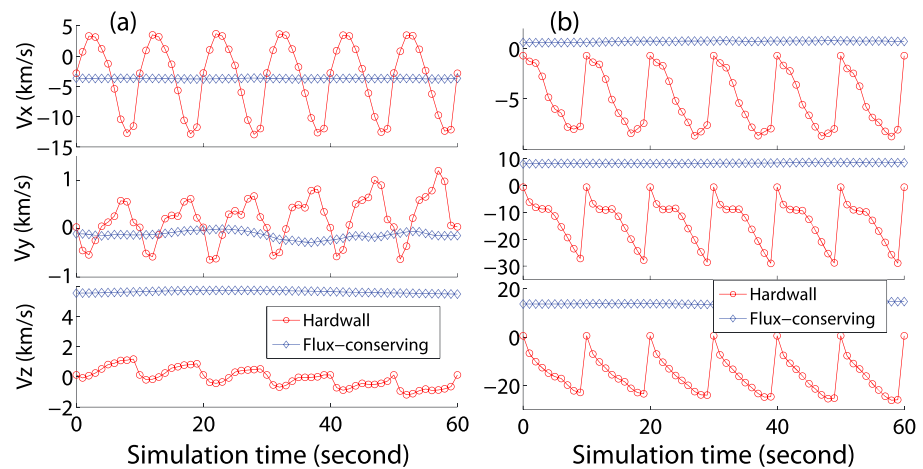


Figure 3. The variations of the three velocity components v_x , v_y , and v_z on the $i = 1$ shell (a) near the north magnetic pole and (b) at $\phi = 17.9^\circ, \theta = 19.7^\circ$ (MLAT = 70.3° , MLT = 13:12) for the two test runs with hardwall (red) and flux-conserving (blue) boundary conditions, respectively.

MIX exchange time occurs at 0, 10, 20, ..., 60 s in this figure. It is clear that the velocity in the hardwall run is driven away from the ionospheric constraint between MIX exchanges, and at the exchange time, the velocity is forced to be the value derived from the ionosphere solver. Consequently, a sudden and artificial jump happens at each exchange time. In contrast, the blue curves in Figure 3 show no such jumps between MIX exchanges for the flux-conserving boundary condition. Fast variations in velocity within the 1 min interval are absent when flux-conserving boundary conditions are used.

In the flux-conserving case, although the velocity conditions in the ghost cells are fixed between the exchange times, the velocities in the $i = 1$ active shell are allowed to evolve with time subject to the constraint on velocity imposed in the ghost cells. Sudden changes in other MHD variables—the density, sound speed, and perturbation magnetic fields—also do not occur. As a result, the FACs that are mapped down to ionosphere to solve the ionosphere equation (7) for the potential distribution change slowly on the exchange time. Thus, no abrupt change appears in the ionospheric potential nor in the magnetospheric velocities on the exchange time scale.

In the region near the north magnetic pole, as shown by Figure 3a, the x component of the convection velocity is always antisunward and the y component of the convection velocity is very close to zero when using the flux-conserving boundary conditions. This behavior is consistent with IMF $B_z = -5$ nT driving during this period. At each MIX exchange time, the x and y velocity components are very close for the two different boundary conditions, which means that the flux-conserving boundary condition constrains the perpendicular velocity in active boundary cells in the polar region to be essentially the mapped ionospheric convection velocity. The velocity becomes very different between MIX exchange times for the standard LFM boundary condition because the constraint of a hardwall boundary in the MHD solver is incompatible with the mapped ionospheric convection velocity. In other regions, such as Figure 3b, the velocities at exchange times for the two cases are also very different from each other, which indicates that the convection pattern near the low-altitude boundary is very sensitive to the boundary conditions.

To investigate global aspects of this sensitivity in more detail, 1 h average simulation diagnostics have been obtained for various MHD quantities in the first four active grid cells above the low-altitude boundary. These cells use the ghost-cell values for the eighth-order interpolations in the MHD solver, so MHD variables in these cells are expected to be especially sensitive to the boundary conditions. Samples in the 1 h average are acquired from two different sequences: (i) Type 1: 360 samples of the fields recorded at each 10 s MIX exchange time are used to compute the 1 h average and (ii) Type 2: 360 samples of the fields recorded midway between each MIX exchange time are used to compute the 1 h average. In both cases, the 1 h averaging interval is from 7:00 to 8:00 ST.

The Type 1 average convection patterns from cell centers at $i = 1, 2, 3, 4$ for the two test runs are shown in Figure 4. Figure 4 (top) shows the average convection for the hardwall run, and Figure 4 (bottom) shows the

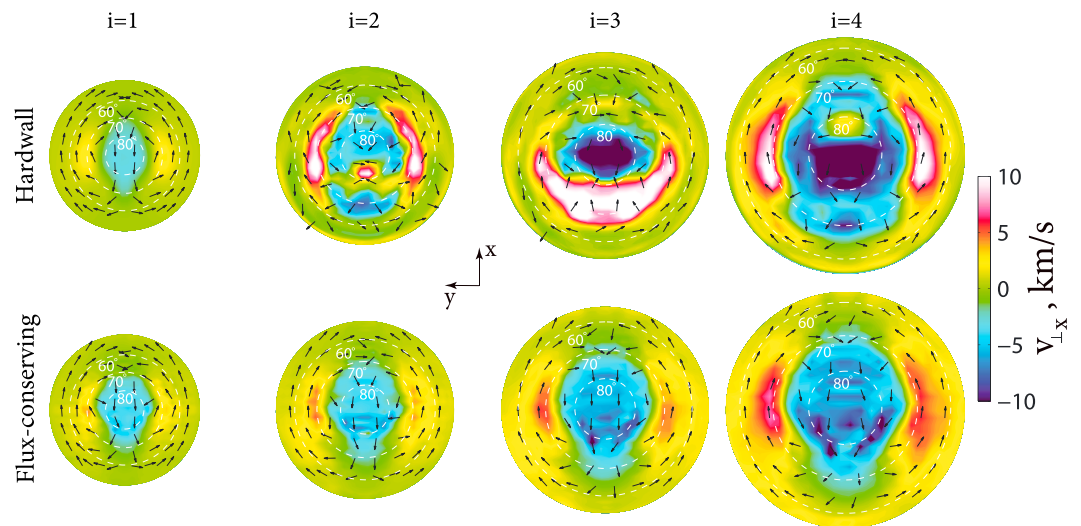


Figure 4. One hour average convection patterns calculated from samples acquired at the MIX exchange time (Type 1 sampling). Average patterns are shown on the first four i shells near the inner boundary for (top) hardwall and (bottom) flux-conserving boundary conditions. The arrows are the directions of perpendicular velocity vectors projected to the x - y plane and color indicates the value of the x component of the perpendicular velocity. The white dashed circles are the ionospheric latitudes mapped to the altitude of the corresponding i shells.

average convection for the flux-conserving run. The arrows in the plots are the directions of perpendicular velocity component projected to the x - y plane, and the color indicates the value of the x component of the perpendicular velocity. The Sun is in the $+x$ direction. The white-dashed circles are the magnetic latitudes at the ionosphere mapped to the altitude of the given i shell.

We can see that when the hardwall boundary condition is used, the average velocity on $i = 1$ forms a regular two-cell convection pattern as expected from the IMF condition $B_z = -5$ nT imposed during the last 4 h of the run. However, when we look at the higher altitudes such as $i = 2$ or $i = 3$, the convection patterns are very different from the pattern on $i = 1$. The $i = 2$ pattern has a patch of positive velocity at 80° latitude on the nightside, while the $i = 3$ pattern has a huge pattern of positive velocity between about 65° and 75° latitude on the nightside and a large negative velocity inside 80° latitude. The convection pattern becomes a more regular two-cell pattern again only at a higher altitude at $i = 4$.

In contrast, when using the flux-conserving boundary conditions, the velocity near the low-altitude boundary has a regular two-cell convection pattern in all four i shells (Figure 4, bottom), and the convection patterns for the different i shells are very consistent with each other. This behavior means that the boundary conditions in ghost cells are properly constraining the solution in flux-conserving run, while the convection near the low-altitude boundary in hardwall run is compromised when downward velocities from higher altitude reflects on the hardwall at $2R_E$, and override the effects of the driving IMF conditions.

Type 2 average convection patterns are shown in Figure 5. Figure 5 (top) shows the patterns for hardwall run. The results differ from those in Figure 4 with the pattern on the $i = 1$ shell no longer exhibiting a two-cell convection. Instead, a large positive velocity pattern occurs between 60° and 70° latitude on the nightside. Also, a patch of positive velocity appears on the dayside perhaps in association with downflows in the cusp. The positive return convection on both the dawnside and duskside between 60° and 70° latitude is absent. The patterns on $i = 2, 3, 4$ shells are also very different from those in Figure 4. In contrast, the convection patterns for flux-conserving boundary conditions are practically identical for Type 1 and Type 2 averaging. These comparisons for the two different averaging intervals indicate that convection near the inner boundary is not well constrained for the simulation with a hardwall boundary and rapidly evolves away from the MIX convection state imposed at MIX exchange times. In this case, the low-altitude boundary condition serves as an effective source of momentum and energy for the magnetosphere as discussed below. With a flux-conserving boundary condition, the low-altitude boundary is a passive element, similar to a matched impedance load on a transmission line. Convection near the low-altitude boundary is well-constrained in this case and evolves slowly with time while remaining consistent with the MIX ionospheric state.

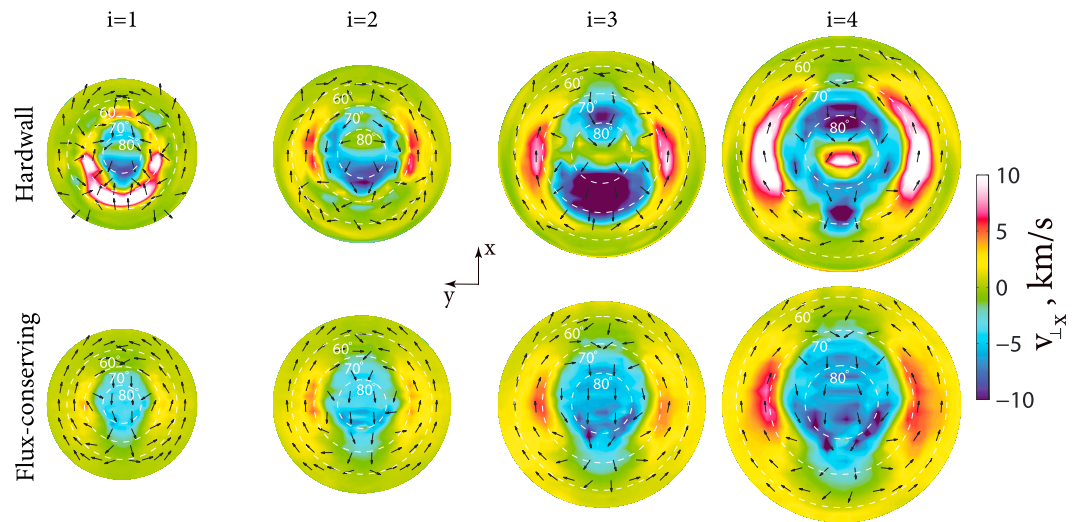


Figure 5. One hour average convection patterns calculated from sample acquired midway between each MIX exchange time (Type 2 sampling) on the first four i shells near the low-altitude boundary for (top) hardwall and (bottom) flux-conserving boundary conditions. The format is the same as Figure 4.

Another improvement resulting from flux-conserving boundary conditions can be seen in the perpendicular current j_{\perp} near the low-altitude boundary. Figure 6 shows the Type 1 average perpendicular current density at exchange times at different altitudes. The first column shows the results on the bottom of $i = 2$ shell ($r = 2.38 R_E$). A large clockwise perpendicular current appears on the nightside for hardwall boundary conditions. The patterns on the bottoms of $i = 3$ ($r = 2.77 R_E$) and $i = 4$ ($r = 3.17 R_E$) show that the perpendicular current density rapidly decreases with increasing distance from the low-altitude boundary. The large perpendicular current density near the low-altitude boundary is a numerical artifact due to the boundary conditions used in this run. Figure 6 (bottom) (flux-conserving boundary conditions) exhibits very little

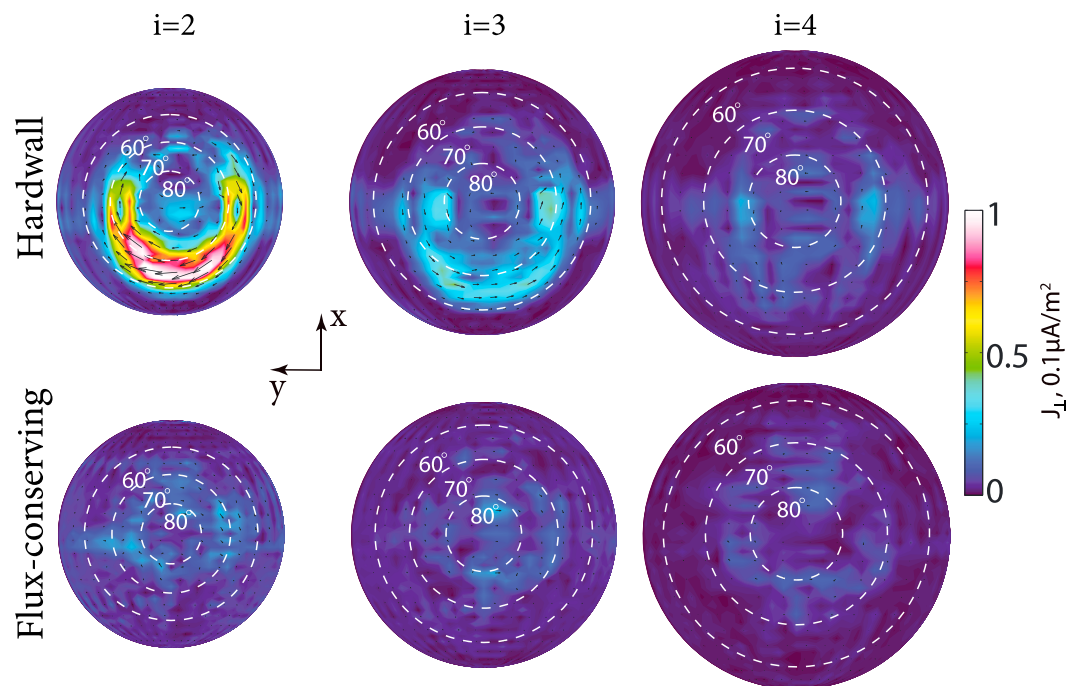


Figure 6. One hour average perpendicular current densities calculated from samples acquired at each MIX exchange time (Type 1 sampling) for (top) hardwall and (bottom) flux-conserving boundary conditions at different altitudes.

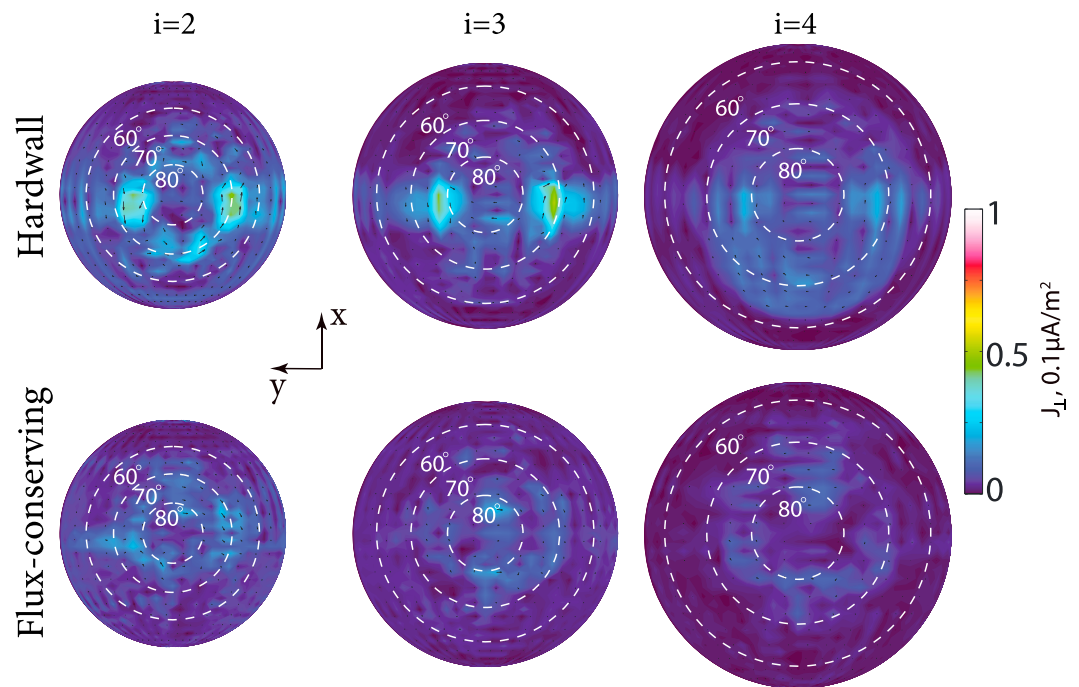


Figure 7. One hour average perpendicular current densities calculated from samples acquired midway between each MIX exchange time (Type 2 sampling) for (top) hardwall and (bottom) flux-conserving boundary conditions at different altitudes.

difference in the pattern and intensity of the perpendicular current density at different altitudes, which is consistent with the zero-perpendicular current condition (equation (3)).

Patterns of Type 2-averaged perpendicular current density are shown in Figure 7. The variation in perpendicular current density with altitude is much smaller for the hardwall boundary condition compared to Type 1 patterns in Figure 6. The patterns of perpendicular current for the flux-conserving boundary conditions are very similar for the two types of averaging (compare Figure 6 and Figure 7). It is not surprising that in the hardwall case, a sudden velocity jump occurs at each exchange time on the first i shell, which effectively transfers momentum to the magnetospheric plasma. The low-altitude magnetosphere must generate a perpendicular current \mathbf{j}_\perp and an associated $\mathbf{j} \times \mathbf{B}$ force to balance the sudden momentum change near the low-altitude boundary. Between each exchange time, the velocity evolves more slowly near the low-altitude boundary (Figure 3), so the perpendicular current is comparatively small. Sudden changes in the velocity do not occur at the exchange time when flux-conserving boundary conditions are used. Thus, the perpendicular current near the low-altitude boundary remains small and well-behaved throughout the run.

3.2. Low-Altitude DC Poynting Flux and Ionospheric Joule Heating

Electromagnetic energy transport is an important aspect of magnetosphere-ionosphere coupling. Electromagnetic energy flows from the magnetosphere as Poynting flux to the ionosphere where it is dissipated as Joule heat. *Weimer* [2005] developed an empirical method for calculating the global distribution of Joule heating from statistical average values of measured perpendicular electric and magnetic fields. An equipotential Boundary Poynting Flux (EBPF) theorem was proposed by *Richmond* [2010] for quasi-static electromagnetic fields, which says that for a volume of ionosphere bounded on the sides by equipotential surfaces, the integrated downward Poynting flux over the top of the volume equals the Joule dissipation within the volume. Later, *Vanhamäki et al.* [2012] showed that there is an exact pointwise matching between the Poynting flux and Joule heating for the case of uniform ionospheric Hall and Pedersen conductances. However, if there are conductance gradients, the pointwise matching will be broken and only Richmond's EBPF theorem is valid for the relationship between the Poynting flux and ionospheric Joule heating.

In the simulations presented here, the Pedersen and Hall conductances are uniform ($\Sigma_p = 5 \text{ S}$, $\Sigma_H = 0$). In addition, in the gap region, field-aligned potential drops are neglected; thus, there is no Joule dissipation

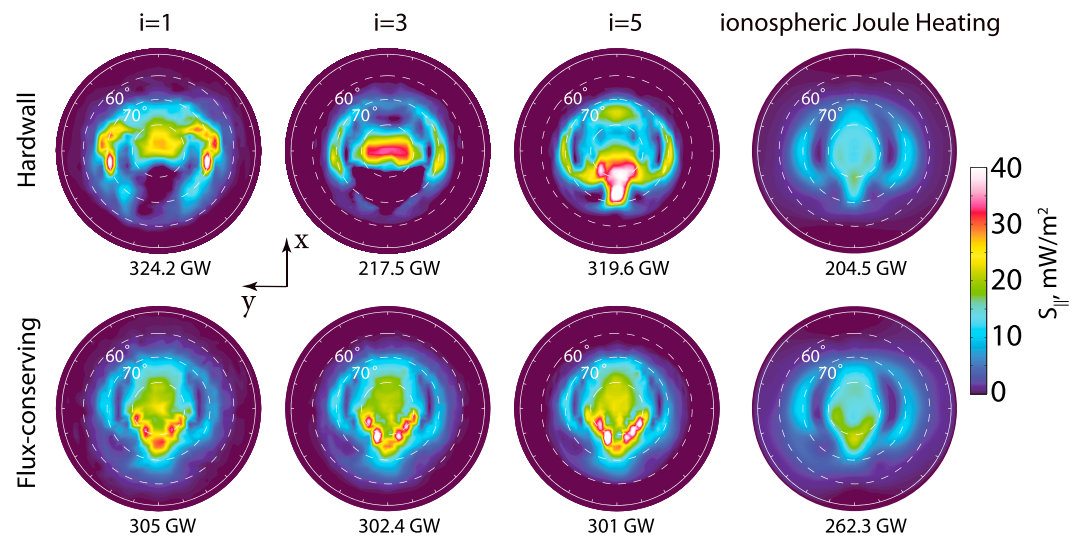


Figure 8. One hour average downward field-aligned (DC) Poynting flux calculated from samples acquired at each MIX exchange time (Type 1 sampling) on the $i = 1, 3, 5$ shells mapped to the ionosphere. The last column shows 1 h average distribution of ionospheric Joule heat on the same scale. The numbers below each plots are the hemispheric integrated power.

from the potential drop. From *Vanhamäki et al.* [2012], for the simulation results presented here, the downward DC field-aligned Poynting flux mapped along magnetic field lines to the ionosphere should pointwise match the ionospheric Joule dissipation. Figure 8 shows the downward DC Poynting flux (i.e., 1 h average Poynting flux) distributions on i shells 1, 3, 5 mapped to the ionosphere as well as the ionospheric Joule Heating (rightmost column). Figure 8 (top) shows the Type 1 average downward DC Poynting flux and Joule heat for the test run with hardwall boundary conditions. The patterns of mapped DC Poynting flux on different i shells, including the patterns on $i = 2$ and 4, which are not shown here, are significantly different. The pattern of downward DC Poynting flux mapped to the ionosphere from $i = 5$ most closely resembles the distribution of Joule heat, but the mapped intensity is almost 50% larger than the Joule heating rate. Figure 8 (bottom) shows the corresponding results for the test run with the flux-conserving boundary conditions. Now, the mapped DC Poynting flux patterns vary little between i shells, including $i = 2$ and 4, and they are also very similar to the Joule dissipation pattern in the ionosphere. The hemispheric integrated downward power for hardwall boundary conditions for $i = 1, 2, \dots, 5$ shells is 324.2 GW, 181.7 GW, 217.5 GW, 266.4 GW, and 319.6 GW, respectively. The hemispheric integrated power for the hardwall condition decreases from the $i = 1$ to $i = 2$ shell; then it progressively increases from $i = 3$ to 5. The simulation of electromagnetic energy transport is not reliable near the low-altitude boundary for this case. In the second case, for flux-conserving boundary conditions, the mapped and integrated hemispheric power flowing downward as DC Poynting flux between i shells (305 GW, 305.3 GW, 302.4 GW, 308.6 GW, and 301 GW for $i = 1, 2, \dots, 5$ shells, respectively) is almost constant to within a few percent and is only 14.7–17.7% larger than the ionospheric Joule heating rate. Ideally, for the specific conditions used here, the DC power flowing down along field lines into the ionosphere should be exactly the same as the ionospheric Joule heat both for spatial distributions and for integrated values. However, some differences remain in both the distributions and the intensity of the power. This discrepancy is caused by the coarse grid and the interpolations used when setting the boundary conditions on the perturbation magnetic field in the ghost cells and when solving the ionospheric potential equation (7). In the hardwall case, the total upward DC Poynting flux for $i = 1, 2, \dots, 5$ shells is 5.1 GW, 181.7 GW, 50.4 GW, 3 GW, and 0.6 GW, respectively. For $i = 2, 3$, the upward DC power is large, which may be caused by the velocity conditions in the hardwall run. In contrast, in the flux-conserving case, the total upward DC Poynting flux for $i = 1, 2, \dots, 5$ shells is 0.5 GW, 0.2 GW, 0.1 GW, 0.2 GW, and 0.9 GW, respectively. In the flux-conserving case, the upward DC Poynting power is negligible compared with the downward DC Poynting power.

3.3. Low-Altitude Alfvénic Poynting Flux

Figure 9 shows 1 h average distributions of Alfvénic Poynting flux on the first five i shells mapped to the ionosphere for both of the test runs. The Alfvénic Poynting flux is calculated using band-pass-filtered

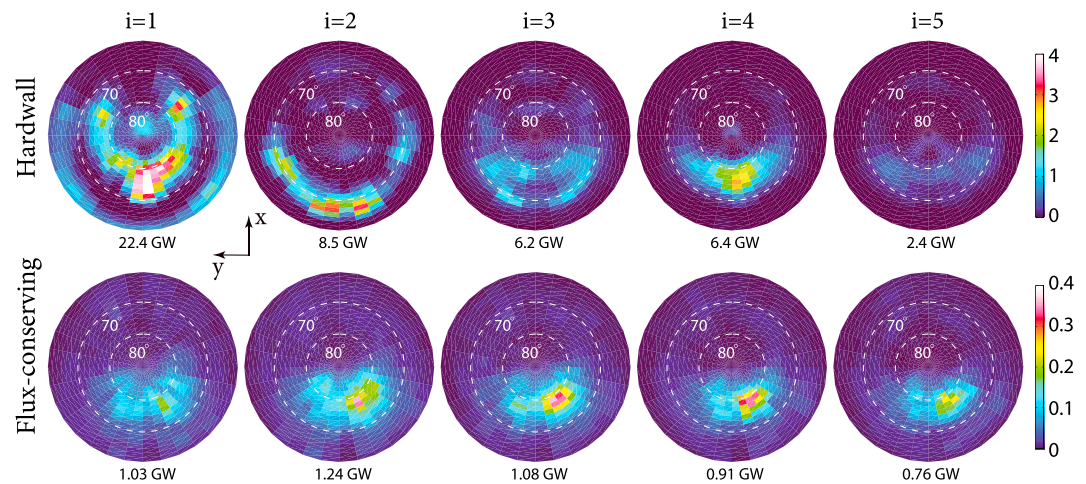


Figure 9. One hour average of downward Alfvénic Poynting flux on $i = 1, 2, \dots, 5$ shells mapped to ionosphere for (top) hardwall boundary and (bottom) flux-conserving boundary. The numbers below each plots are the hemispheric integrated Alfvénic power.

perturbation electric and magnetic fields following the method of *Zhang et al.* [2012]. The parallel component of the Alfvénic Poynting flux is

$$S_{ac} = \frac{1}{\mu_0} \delta \mathbf{E} \times \delta \mathbf{B} \cdot \frac{\mathbf{B}_{avg}}{|\mathbf{B}_{avg}|}, \quad (13)$$

where B_{avg} is a 180 s running average of the local magnetic field. The time assigned to the value of \mathbf{B}_{avg} is the time at the end of the 180 s averaging window. $\delta \mathbf{E}$ and $\delta \mathbf{B}$ are the perturbation electric and magnetic fields calculated as the difference between the instantaneous (saved) value and the average value. The simulation data are saved every 5 s. Thus, there are 720 data points in 1 h. Each plot in Figure 9 is an average of 720 “instantaneous” patterns. After the parallel Alfvénic Poynting fluxes on different i shells are obtained from (13), the resulting values are dipole mapped to the ionosphere to a reference altitude of 120 km assuming S_{ac}/B_d is constant along field lines.

As seen from the top patterns of Figure 9, significant Alfvénic Poynting flux flows downward toward the ionosphere from $i = 1, 2, 3, 4$ shells. Less downward power flows from the $i = 5$ shell. Also the pattern at each i shell is very different from the one at other i shells. The Alfvénic Poynting flux is significantly affected by the hardwall boundary conditions used in this run. Alfvénic Poynting flux is not conserved along field lines when using the hardwall boundary. In contrast, the patterns in Figure 9 (bottom) for flux-conserving boundary conditions are very similar to each other on all i shells. However, the peak intensity of the Poynting flux progressively decreases with decreasing i shell, while the integrated power increases from 1.03 GW at $i = 1$ to 1.24 GW at $i = 2$ then progressively decreases to 0.76 GW at $i = 5$. Some of this variation is a grid effect and occurs because the magnetic flux tubes converge faster than the numerical grid at lower altitude. Consequently, the numerical grid inadequately resolves Alfvén waves with perpendicular lengths comparable to the grid size. The result is numerical dissipation of Alfvén power closer to the low-altitude boundary, and less Alfvénic power on i shells closer to the low-altitude boundary. Despite this numerical dissipation, the Alfvénic Poynting flux is conserved within 25% referenced to $i = 1$ shell, when using the flux-conserving boundary condition rather than for the standard LFM boundary condition.

3.4. Ionospheric and Magnetospheric Patterns

One hour average ionospheric patterns for electric potential and field-aligned current, and the number flux and energy flux of precipitating electrons derived from LFM’s electron precipitation model [*Wiltberger et al.*, 2004], are shown in Figure 10. The total downward field-aligned current for the case with hardwall boundary conditions is 2.82 MA, which is smaller than the run with flux-conserving boundary conditions, for which the total downward current is 2.95 MA. As discussed in section 3.1, large perpendicular currents develop near the inner boundary to maintain force balance when the velocity is reset on $i = 1$ at the MIX exchange time. This perpendicular current is evidently fed by diversion of some field-aligned current, which reduces the FAC reaching the ionosphere in the hardwall run relative to that in the flux-conserving run. For

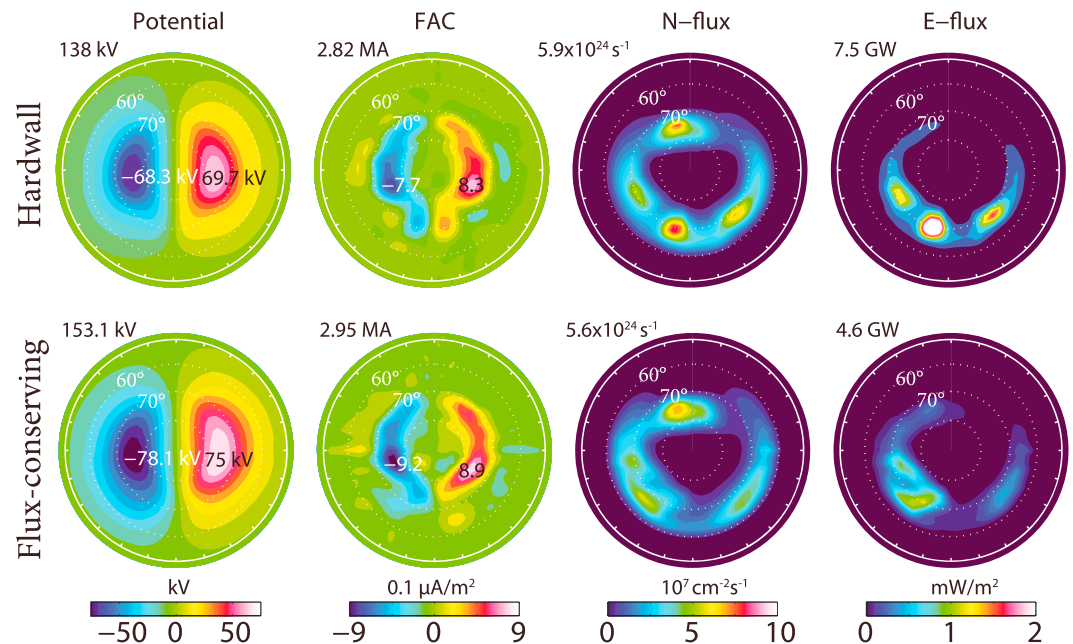


Figure 10. One hour average ionospheric variables for (top) hardwall and (bottom) flux-conserving boundary conditions. The numbers on the top left corner in each plot are the cross polar cap potential, integrated hemispheric downward current, and the hemispheric rates of electron precipitating number and energy, respectively.

flux-conserving boundary conditions, most of the field-aligned current flows through the inner boundary without diversion. The cross polar cap potential (CPCP) for the two cases are 138 kV and 153.1 kV, respectively. Region 2 currents are relatively weak in both cases so most of the field-aligned current must close across the polar cap. The larger FAC in the flux conserving run is thus consistent with its larger CPCP since the conductance ($\Sigma_p = 5 S$) is the same for both runs. The integrated hemispheric number flux of precipitating electrons deduced from LFM's precipitation model is bigger for the hardwall run ($5.9 \times 10^{24} s^{-1}$) relative to the flux-conserving run ($5.6 \times 10^{24} s^{-1}$). The integrated hemispheric energy flux of precipitating electrons is larger for the hardwall run (7.6 GW) than for the flux-conserving run (4.6 GW). This larger energy flux for the hardwall run may also be caused by the large artificial perpendicular current near the inner boundary discussed in section 3.1. Because the large perpendicular current flows on the nightside are clockwise (Figure 6), which is basically in the direction of the electric field, additional Joule dissipation ($\mathbf{j}_\perp \cdot \mathbf{E}_\perp$) occurs near the low-altitude boundary, which increases the plasma energy there. Thus, for the hardwall run, the precipitating electron energy, which is established by the value on the bottom of $i = 2$ shell, is higher than for the flux-conserving run. As a result, the energy flux for the hardwall run is larger than for the flux-conserving run.

Figure 11 shows the one hour average density distribution in the magnetospheric equatorial plane for both test runs. The white arrows are the velocity vectors projected onto the equatorial plane. The white curves show the $B_z = 0$ contours. The case with flux-conserving boundary conditions has a slightly thinner magnetosheath and higher density in the inner magnetosphere. The extra density in the inner magnetosphere may be due to the numerical diffusion from ghost cells, since the boundary is no longer a hardwall for plasma. The density depletion in the inner magnetosphere sunward of earth is a factor of 10 higher when the flux-conserving boundary conditions are imposed. The average upward fluence entering the MHD domain for the whole Northern Hemisphere at $i = 1$ is 8.27×10^{23} ions/s for IMF $B_z = -5$ nT, which is an order of magnitude smaller than the quiet time outflow fluence reported by *Yau and André* [1997]. The average downward fluence at the boundary is 3.58×10^{24} ions/s, which results in a net downward fluence of 2.75×10^{24} ions/s, mainly in the cusp region and midlatitude nightside region (55° – 65° MLAT). The diffusion of plasma from ghost cells into the magnetosphere evidently also occurs for de facto outflow boundary conditions in BATS-R-US [*Wellington and Liemohn*, 2014]. The location of the magnetopause for the flux-conserving case is a little further out than for the hardwall case. The locations of the $B_z = 0$ contours are not significantly different for the two cases. However, local differences up to $3 R_E$ on the nightside may

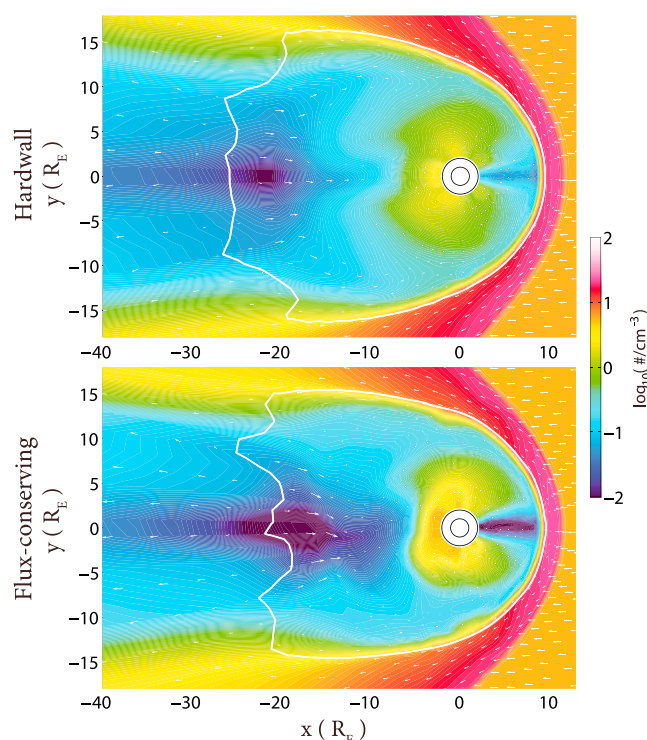


Figure 11. One hour average equatorial distribution of number density for (top) hardwall and (bottom) flux-conserving boundary conditions. The arrows in the plots are the velocity vectors projected to the equatorial plane. The white curves denote $B_z = 0$.

physically consistent fields near the low-altitude simulation boundary compared to the standard hardwall boundary conditions used in the LFM model. First, the artificial effects caused by periodically overwriting the velocity in the active boundary cell at the magnetosphere-ionosphere exchange are eliminated by imposing the velocity boundary conditions in ghost cells. The artificial effects that appear at the exchange time include velocity jumps and perpendicular currents near the low-altitude boundary. Second, the artificial effects caused by hardwall boundary conditions disappear when using a flux-conserving boundary condition. Convection patterns near the low-altitude boundary are properly regulated and are consistent at different altitudes. The Alfvénic Poynting flux is better conserved but some anomalies in integrated power remains, possibly due to numerical dissipation caused by the grid. The field-aligned DC Poynting flux is also conserved along field lines. Comparison of the DC Poynting flux with the ionospheric Joule heating rate shows that the flux-conserving method preserves the theorems described by *Richmond* [2010] and *Vanhamäki et al.* [2012] within 15%, and flux-conserving boundary conditions make the low-altitude boundary relatively transparent to the flow of electromagnetic energy across it. The DC electromagnetic energy flux incident on the boundary is dissipated in the ionosphere.

Besides the two simulations presented in this paper, two additional simulations that use boundary conditions partly from the hardwall or flux-conserving conditions were done (see supporting information for the paper). The first one uses the density, sound speed, and magnetic field boundary conditions from the hardwall case (symmetric across boundary) but the velocity condition from flux-conserving run. The second one uses the density, sound speed, and velocity boundary conditions from the flux-conserving run, and only the magnetic field boundary condition (symmetric across boundary) from the hardwall run. Comparing the simulation results from the four cases, the velocity boundary condition is most important for the convection and energy distributions in the magnetosphere near the inner boundary. Together with the velocity boundary condition, the magnetic field boundary condition greatly affects the energy transmission from magnetosphere through the boundary to ionosphere and the intensity of FAC. As might be expected, the density and sound speed conditions mainly affect the density profiles in the inner magnetosphere.

indicate that the nightside reconnection process is affected by the different low-altitude boundary conditions. The low-density region near $x = -20 R_E$, $y = 0$ in the case with flux-conserving boundary conditions has a greater spatial extent than the hardwall case. Although some differences are apparent in the magnetospheric properties, the two solutions in the magnetosphere far away from the low-altitude boundary are not very different from each other.

4. Summary

In this paper, we developed a method to specify flux-conserving boundary conditions for electromagnetic energy flowing through the low-altitude boundary in global magnetospheric MHD models. Simulations with idealized upstream solar wind input have been performed using the LFM simulation model with both standard hardwall boundary conditions and flux-conserving boundary conditions. The results show that flux-conserving boundary conditions produce phys-

In conclusion, flux conserving boundary conditions for global MHD models have been developed. Improved results near the inner boundary have been achieved by using the newly developed boundary conditions. The MI coupling is shown to be more consistent in the context of electromagnetic energy conservation. The implementation in this paper is described for one-fluid MHD, but extension to multifluid MHD models is straightforward.

Acknowledgments

The research was supported by NASA grants NNX11AO59G and NNX14AN52G. Computing resources were provided by NCAR CISL grants 36761008 and 2761009. NCAR is supported by the NSF. Simulation data are available from Sheng Xi or William Lotko (william.lotko@dartmouth.edu).

Michael Liemohn thanks You-Qiu Hu and Ilja Honkonen for their assistance in evaluating this paper.

References

- Brambles, O. J., W. Lotko, P. A. Damiano, B. Zhang, M. Wiltberger, and J. Lyon (2010), Effects of causally driven cusp O^+ outflow on the storm time magnetosphere-ionosphere system using a multifluid global simulation, *J. Geophys. Res.*, *115*, A00J04, doi:10.1029/2010JA015469.
- Brecht, S. H., J. G. Lyon, J. A. Fedder, and K. Hain (1982), A time dependent three-dimensional simulation of the Earth's magnetosphere: Reconnection events, *J. Geophys. Res.*, *87*(A8), 6098–6108, doi:10.1029/JA087iA08p06098.
- Fedder, J. A., and J. G. Lyon (1987), The solar wind-magnetosphere-ionosphere current-voltage relationship, *Geophys. Res. Lett.*, *14*(8), 880–883, doi:10.1029/GL014i008p00880.
- Frank, L. A., et al. (1995), Observations of plasmas and magnetic fields in Earth's distant magnetotail: Comparison with a global MHD model, *J. Geophys. Res.*, *100*(A10), 19,177–19,190, doi:10.1029/95JA00571.
- Gallagher, D. L., P. D. Craven, and R. H. Comfort (2000), Global core plasma model, *J. Geophys. Res.*, *105*(A8), 18,819–18,833, doi:10.1029/1999JA000241.
- Garcia, K. S., V. G. Merkin, and W. J. Hughes (2010), Effects of nightside O^+ outflow on magnetospheric dynamics: Results of multifluid MHD modeling, *J. Geophys. Res.*, *115*, A00J09, doi:10.1029/2010JA015730.
- Glocer, A., G. Tóth, Y. Ma, T. Gombosi, J.-C. Zhang, and L. M. Kistler (2009), Multifluid block-adaptive-tree solar wind roe-type upwind scheme: Magnetospheric composition and dynamics during geomagnetic storms—Initial results, *J. Geophys. Res.*, *114*, A12203, doi:10.1029/2009JA014418.
- Goodman, M. L. (1995), A three-dimensional, iterative mapping procedure for the implementation of an ionosphere-magnetosphere anisotropic Ohm's law boundary condition in global magnetohydrodynamic simulations, *Ann. Geophys.*, *13*, 843–853, doi:10.1007/s00585-995-0843-z.
- Hu, Y. Q., X. C. Guo, and C. Wang (2007), On the ionospheric and reconnection potentials of the Earth: Results from global MHD simulations, *J. Geophys. Res.*, *112*, A07215, doi:10.1029/2006JA012145.
- Janhunen, P., M. Palmroth, T. Laitinen, I. Honkonen, L. Juusola, G. Fackó, and T. Pulkkinen (2012), The GUMICS-4 global MHD magnetosphere-ionosphere coupling simulation, *J. Atmos. Sol. Terr. Phys.*, *80*, 48–59, doi:10.1016/j.jastp.2012.03.006.
- Leboeuf, J. N., T. Tajima, C. F. Kennel, and J. M. Dawson (1978), Global simulation of the time-dependent magnetosphere, *Geophys. Res. Lett.*, *5*(7), 609–612, doi:10.1029/GL005i007p00609.
- Lotko, W. (2004), Inductive magnetosphere-ionosphere coupling, *J. Atmos. Sol. Terr. Phys.*, *66*(15–16), 1443–1456, doi:10.1016/j.jastp.2004.03.027, towards an Integrated Model of the Space Weather System.
- Lyon, J., S. H. Brecht, J. A. Fedder, and P. Palmadesso (1980), The effects on the Earth's magnetotail from shocks in the solar wind, *Geophys. Res. Lett.*, *7*(9), 721–724, doi:10.1029/GL007i009p00721.
- Lyon, J., J. Fedder, and C. Mobarry (2004), The Lyon-Fedder-Mobarry (LFM) global MHD magnetospheric simulation code, *J. Atmos. Sol. Terr. Phys.*, *66*(15–16), 1333–1350, doi:10.1016/j.jastp.2004.03.020.
- Merkin, V. G., and J. G. Lyon (2010), Effects of the low-latitude ionospheric boundary condition on the global magnetosphere, *J. Geophys. Res.*, *115*, A10202, doi:10.1029/2010JA015461.
- Ogino, T. (1986), A three-dimensional MHD simulation of the interaction of the solar wind with the Earth's magnetosphere: The generation of field-aligned currents, *J. Geophys. Res.*, *91*(A6), 6791–6806, doi:10.1029/JA091iA06p06791.
- Powell, K. G., P. L. Roe, T. J. Linde, T. I. Gombosi, and D. L. D. Zeeuw (1999), A solution-adaptive upwind scheme for ideal magnetohydrodynamics, *J. Comput. Phys.*, *154*(2), 284–309, doi:10.1006/jcph.1999.6299.
- Raeder, J. (2003), Global magnetohydrodynamics—A tutorial, in *Space Plasma Simulation, Lecture Notes in Physics*, vol. 615, edited by J. Raeder, pp. 212–246, Springer, Berlin, doi:10.1007/3-540-36530-3_11.
- Richmond, A. D. (2010), On the ionospheric application of Poynting's theorem, *J. Geophys. Res.*, *115*, A10311, doi:10.1029/2010JA015768.
- Russell, C. T. (1971), Geophysical coordinate transformations, *Cosmic Electrodynamic*, *2*, 184–196.
- Tanaka, T. (1995), Generation mechanisms for magnetosphere-ionosphere current systems deduced from a three-dimensional MHD simulation of the solar wind-magnetosphere-ionosphere coupling processes, *J. Geophys. Res.*, *100*(A7), 12,057–12,074, doi:10.1029/95JA00419.
- Tóth, G., et al. (2012), Adaptive numerical algorithms in space weather modeling, *J. Comput. Phys.*, *231*(3), 870–903, doi:10.1016/j.jcp.2011.02.006, Special issue: Computational Plasma Physics Special Issue: Computational Plasma Physics.
- Vanhamäki, H., A. Yoshikawa, O. Amm, and R. Fujii (2012), Ionospheric joule heating and Poynting flux in quasi-static approximation, *J. Geophys. Res.*, *117*, A08327, doi:10.1029/2012JA017841.
- Walker, R. J., M. Ashour-Abdalla, M. El Alaoui, and F. V. Coroniti (2006), Magnetospheric convection during prolonged intervals with southward interplanetary magnetic field, *J. Geophys. Res.*, *111*, A10219, doi:10.1029/2005JA011541.
- Weimer, D. R. (2005), Improved ionospheric electrodynamic models and application to calculating joule heating rates, *J. Geophys. Res.*, *110*, A05306, doi:10.1029/2004JA010884.
- Welling, D. T., and M. W. Liemohn (2014), Outflow in global magnetohydrodynamics as a function of a passive inner boundary source, *J. Geophys. Res. Space Physics*, *119*, 2691–2705, doi:10.1002/2013JA019374.
- Wiltberger, M., W. Wang, A. Burns, S. Solomon, J. Lyon, and C. Goodrich (2004), Initial results from the coupled magnetosphere ionosphere thermosphere model: Magnetospheric and ionospheric responses, *J. Atmos. Sol. Terr. Phys.*, *66*(15–16), 1411–1423, doi:10.1016/j.jastp.2004.03.026, towards an Integrated Model of the Space Weather System.
- Wiltberger, M., W. Lotko, J. G. Lyon, P. Damiano, and V. Merkin (2010), Influence of cusp O^+ outflow on magnetotail dynamics in a multifluid MHD model of the magnetosphere, *J. Geophys. Res.*, *115*, A00J05, doi:10.1029/2010JA015579.
- Winglee, R. M., W. Lewis, and G. Lu (2005), Mapping of the heavy ion outflows as seen by image and multifluid global modeling for the 17 April 2002 storm, *J. Geophys. Res.*, *110*, A12524, doi:10.1029/2004JA010909.
- Yau, A., and M. André (1997), Sources of ion outflow in the high latitude ionosphere, *Space Sci. Rev.*, *80*(1–2), 1–25, doi:10.1023/A:1004947203046.
- Zhang, B., W. Lotko, O. Brambles, P. Damiano, M. Wiltberger, and J. Lyon (2012), Magnetotail origins of auroral Alfvénic power, *J. Geophys. Res.*, *117*, A09205, doi:10.1029/2012JA017680.